Electronic Supplementary Information

Remarkable Enhancement of Optical and Electric Properties by Temperature-controlled Solid-phase Molecular Motion

Meng-Meng Lun, ‡[a] Chang-Yuan Su, ‡[a] Qiang-Qiang Jia,[b] Zhi-Xu Zhang,[b] Jie Li,[a] Hai-Feng Lu, *[b] Yi Zhang *[b] and Da-Wei Fu *[ab]

[a] Ordered Matter Science Research Center, Jiangsu Key Laboratory for Science and Applications of Molecular Ferroelectrics, Southeast University, Nanjing, 211189, P. R. China

[b] Institute for Science and Applications of Molecular Ferroelectrics, Key Laboratory of the Ministry of Education for Advanced Catalysis Materials, Zhejiang Normal University, Jinhua, 321004, P. R. China.

‡ These authors contributed equally.

Corresponding author (E-mail: luhaifeng@zjnu.edu.cn; yizhang1980@seu.edu.cn; dawei@seu.edu.cn)

Experimental section

Preparation of compounds

All chemicals, including 15-crown-5, 18-crown-6, perchloric acid ($HClO_4$, 70 wt.% in H_2O), *N*,*N*-dimethylethylenediamine ($Me_2N(CH_2)_2NH_2$) and methanol (MeOH), were purchased and used without further purification. These crown ether-based supramolecules were prepared by the simple solution method. As illustrated in Fig. S1, the perchloric acid, *N*,*N*-dimethylethylenediamine and crown ether molecules with a molar ratio of *x*: 1: 1 (*x* = 1, 2) were sequentially dissolved in a mixed solution of MeOH and H_2O with a volume ratio of 1:1 to become the precursor solution. Whereafter, as the precursor solution slowly evaporates at room temperature, many colorless crystals are obtained in the beaker.

Characterization

Single-crystal X-ray Diffraction (SC-XRD). The crystallographic structures of these four supramolecules were identified by using a Rigaku single-crystal X-ray

diffractometer with Mo-Kα radiation (λ = 0.71073 Å). The structures of samples were determined by direct methods and refined by the full matrix method through the SHELXTL software package. All non-hydrogen atoms were refined anisotropically, and all hydrogen atoms which were generated geometrically possessed isotropic displacement parameters. The crystallographic information and structure refinement of samples are summarized in Table S2. Moreover, the crystallographic structures of these supramolecules have been deposited at the Cambridge Crystallographic Data Center (CCDC) (deposition numbers: 2212389-2212393) and can be obtained free of charge from the CCDC *via* www.ccdc.cam.ac.uk/getstructures.

Powder X-ray Diffraction (PXRD). The powder X-ray diffraction patterns of microcrystalline samples were characterized by using a Rigaku D-MAX diffraction system using Cu-kα radiation in the 2θ range from 5° to 50° with a step size of 0.02° at 298 K. Simulated powder patterns of samples were calculated by Mercury software package using the crystallographic information file from the single-crystal X-ray experiment.

Infrared (IR) Spectroscopy. The IR spectra of these four supramolecules were performed at room temperature using a Shimadzu IR-60 spectrometer in the range from 4000 to 400 cm^{-1}.

Dielectric. For dielectric characterization, these crystals of supramolecules were ground to become powders and then pressed into a plate with 0.5 mm thickness. Both plate surfaces were coated with silver paste and dried in an oven at 333 K for 5 h. The plate was then used as an electrode to record the curve of temperature-dependent dielectric permittivity ε by a Tonghui TH2828A Precision LCR meter with an AC voltage of 1 V. Meanwhile, the dielectric permittivity on single-crystal samples along different crystallographic axes was measured, and the crystallographic axes of a single crystal for **4** were determined as follows: firstly, selecting the as-grown single crystals according to the simulated crystal shape from Mercury software based on the crystallographic data of **4**; secondly, applying PXRD measurement to ascertain a few lattice planes; finally, the crystallography axis of **4** can be determined. The complex dielectric permittivity ε ($\varepsilon = \varepsilon' - \varepsilon''$), where ε' is the real part, and ε'' is the imaginary part.

Differential Scanning Calorimetry (DSC). DSC measurements of these four supramolecules were performed by a NETZSCH-214 instrument, and microcrystalline samples were heated and cooled in an aluminum crucible with a rate of 20 K/min.

Second Harmonic Generation (SHG). SHG signals of polycrystalline samples for **3**

and **4** were recorded by an Edinburgh FLS920 instrument equipped with an Nd:YAG laser (λ = 1064 nm, Vibrant 355 II, OPOTEK), which can emit unexpanded laser beam with low divergence. In addition, polycrystalline samples of **4** were also ground and sieved into the different particle size ranges: 38-50 μm, 50-75 μm, 75-100 μm, 100-150 μm, 150-200 μm, and 200-300 μm. Meanwhile, KH_2PO_4 Crystals were ground and sieved into the same particle size ranges as **4** and used as references. More importantly, the SHG signal intensity on single-crystal samples along different crystallographic axes was measured at room temperature. The crystallographic axes of a single crystal for **4** were determined as mentioned above.

Macroscopic piezoelectric coefficient measurement. The macroscopic piezoelectric coefficient (d_{33}) of crystals in α or β phases was measured by a commercial piezometer (piezotest, model PM200) using the "Berlincourt" method (namely "quasi-static" method). Under the assistance of a heat gun, the single crystal was heated up to 370 K, and the temperature was detected by a thermocouple sensor. Multiple single crystals were measured to determine the d_{33} of **4** in α and β phases. The crystallographic axes of a single crystal for **4** were determined as mentioned above.

Hirshfeld Surfaces Analysis. Hirshfeld surfaces and the associated 2D fingerprint plots were calculated by the CrystalExplorer software package by inputting the crystallographic structure files of these four supramolecules generated by SC-XRD. Hirshfeld surfaces can provide the information about intermolecular interactions in these four supramolecules. The 2D fingerprint plot is a combination of d_e and d_i that provides the summary of intermolecular contacts in the crystal and are as a useful complement to the Hirshfeld surfaces, where d_i is the distance to the nearest atom center interior to the surface, and d_e exterior to the surface. The normalized contact distance d_{norm} is based on d_e, d_i and the van der Waals (vdW) radii of the two atoms external (r_{e}^{vdW}) and internal (r_{i}^{vdW}) to the surface:

$$d_{norm} = \frac{d_i - r^{vdW}}{r_i^{vdW}} + \frac{d_e - r}{r_e^{vdW}}$$

d_{norm} surface is used for the identification of close intermolecular interactions. The value d_{norm} is negative or positive when intermolecular contacts are shorter or longer than r^{vdW}, respectively. Hirshfeld surface with d_{norm} values display a red-blue-white color scheme: where red regions correspond to closer contacts and negative d_{norm} value; the blue regions correspond to longer contacts and positive d_{norm} value; and the white regions correspond to the distance of contacts is exactly the van der Waals separation and with a d_{norm} value of zero.

Theoretical Calculation. The potential energy and molecular dynamics (MD) of **4**

were performed based on density functional theory (DFT) by using the Materials Studio software package. Firstly, the crystal structures obtained from SC-XRD characterization are further optimized geometrically, by the exchange-correlation interactions within the generalized gradient approximation (GGA) as parameterized on the basis of the Perdew-Burke-Ernzerh (PBE) function. [1] The plane wave cut-off energy of 630 eV and $2 \times 2 \times 2$ k-point mesh is set. Then the single point energies of the optimized model structure for **4** were calculated at every 20° rotation of building blocks around its crystallographic *c*-axis. Secondly, the MD simulations were implemented based on the periodic models, in which all the unit-cell parameters are fixed but all atoms and associated coordinates are free motion during the calculation process. The supramolecular dynamic motion at 293 and 410 K are simulated by the Forcite module with the following parameter settings: the ensemble of the constant-volume&temperature (NVT), the control method of Nose, the forcefield of Dreiding, the summation method of Ewald based, and other default parameters. It is worth noting that Materials Studio software cannot run the CASTEP for the disordered crystal due to technical limitations. According to the technical instruction in Materials Studio software, the current implementation of the molecular dynamic algorithms in CASTEP is not yet compatible with the virtual crystal approximation formalism. None of the Molecule Dynamics (MD) schemes (NVE, NVT, NPT, etc.) works for disordered crystals in the current version. Therefore, the MD simulations of 4 at 293 and 410 K are implemented based on its α phase due to the α and β with the same orthorhombic system and similar crystallographic parameters. Finally, the curves of refractive-index dispersion of **4** along different crystal axes were calculated in CASTEP module.

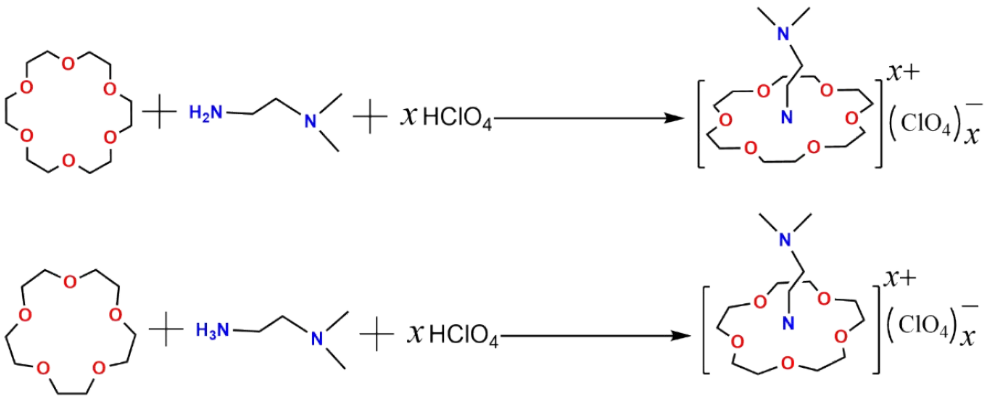

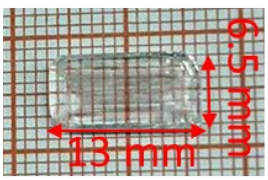

Fig. S1 The preparation of these four supramolecules and x=1, 2. The single crystal is $[(Me_2N(CH_2)_2NH_3)(18\text{-crown-6})]ClO_4$ with the size of 13 mm × 6.5 mm × 1 mm.

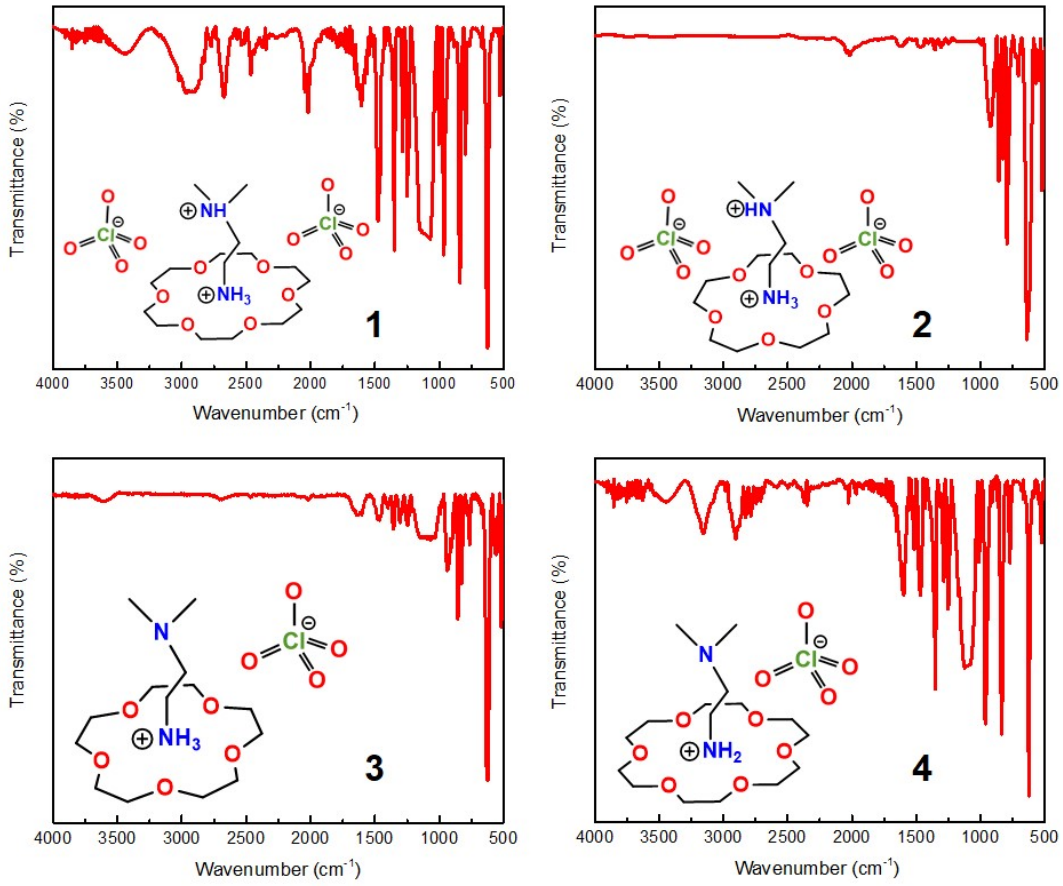

Fig. S2 IR spectra of four supramolecules measured at room temperature. The peaks in the range of 1225-965 and 900-650 cm^{-1} are assigned to the characteristic absorption of crown ether molecules and the bending vibration absorption of -CH_2, respectively; the peaks in the range of 1730-1550 and 3600-3100 cm^{-1} correspond the vibrational absorption of -NH_3 as well as -OH in H_2O, respectively. In addition, the characteristic absorption of ClO_4^- peaks around 1100 cm^{-1}.

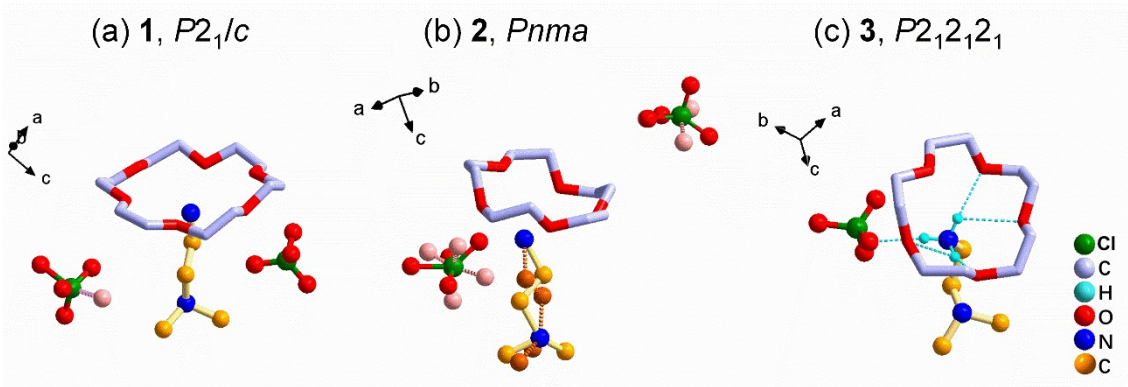

Fig S3 The structural units of **1** (a), **2** (b) and **3** (c) at room temperature.

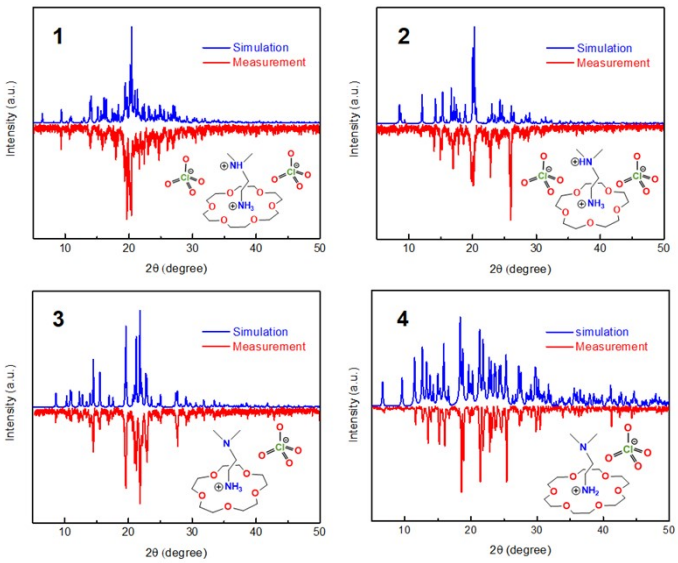

Fig. S4 The measured and simulated PXRD patterns of these four supramolecules at room temperature.

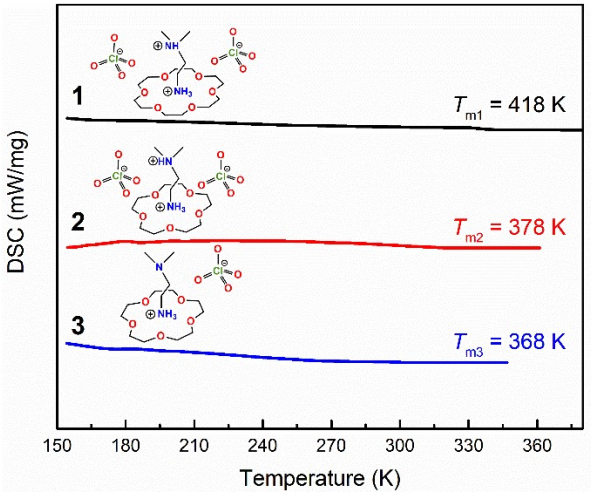

Fig. S5 The curves of DSC and melting points (T_m) for **1**, **2** and **3** upon heating.

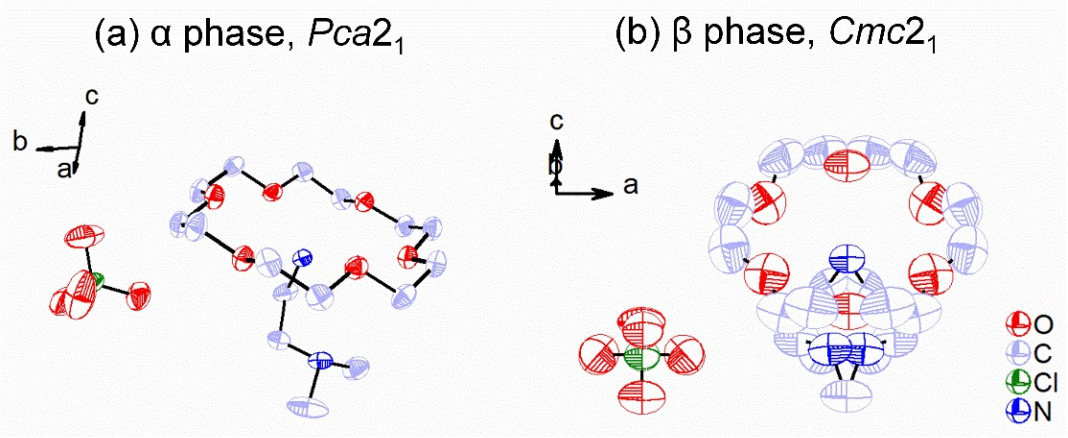

Fig. S6 Displacement ellipsoids of **4** at different temperatures were drawn at the 30% probability level. Hydrogen atoms were omitted for clarity.

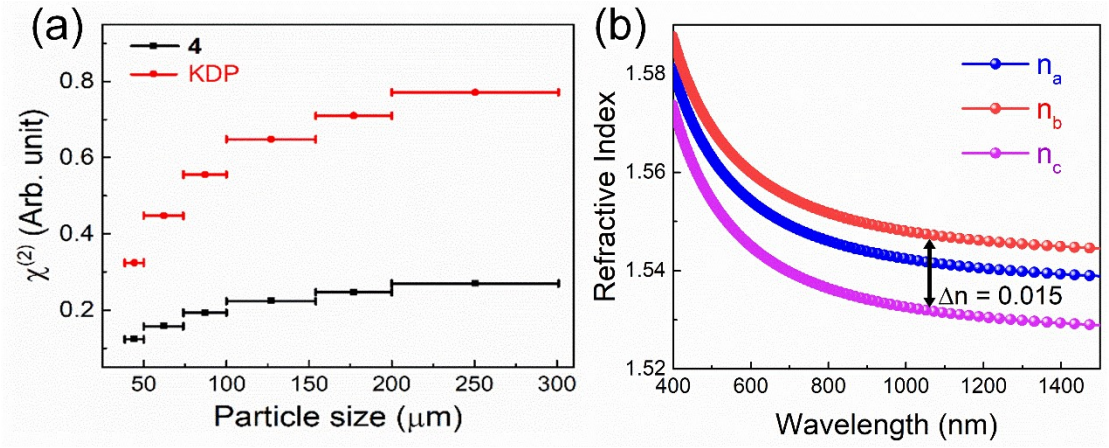

Fig. S7 (a) The second harmonic generation intensity vs particle sizes of **4** under the exaction of 1064 nm laser. (b) Theoretically calculated refractive indices at different wavelengths and birefringence of **4** at 1064 nm.

Analysis: the second harmonic generation (SHG) responses of **4** increase as particle sizes increase in Fig. S7a, indicating that **4** conforms to the type-**I** phase matchable behavior. As shown in Fig. S7b, the calculated refractive indexes of **4** along different crystal axes by Materials Studio software show significant anisotropy, and the birefringence is approximately 0.015 at 1064 nm. In general, the SHG phase-matching condition can be satisfied according to the requirement: $n_{max}(\lambda) > n_{min}(\lambda/2)$, where $n_{max}(\lambda)$ and n_{min} $(\lambda/2)$ are the largest and smallest refractive indices at the fundamental and SHG wavelengths, respectively.[2-4] Fig. R3 displays that the value of $n_{max}(1064)$ and $n_{min}(532)$ for **4** is 1.547 and 1.550, respectively, which thus cannot satisfy the SHG phase-matching condition at 1064 nm. In summary, although **4** possesses SHG response under the exaction of 1064 nm laser, the signal intensity is only 0.3 times that of KDP in the range of 90-150 μm.

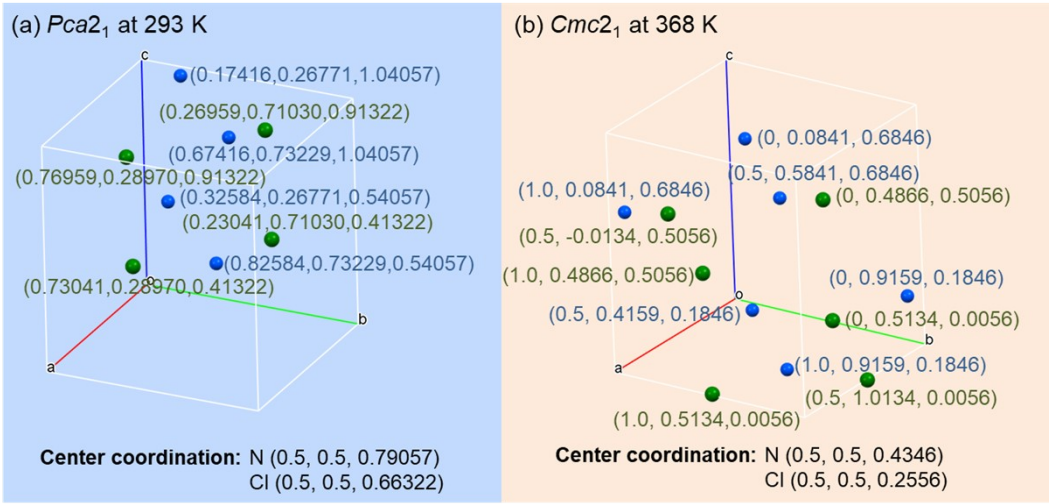

Fig. S8 Atomic coordinates of **4** crystallized α phase (a) and β phase (b) for the calculation of spontaneous polarization (*Ps*) based on the point change model.

According to the crystal structures of **4** at different temperatures, we select a unit cell and assume that the centers of positive and negative charges are located on the N atoms and Cl atoms, respectively. The Ps_1 and Ps_2 for α and β phase are respectively calculated as follows:

Along crystallographic *c*-axis:

$$P_s = \lim \frac{1}{V}\sum q_i r_i = (q_N r_N + q_{Cl} r_{Cl})/V$$

$$P_{s1} = 4 \times (e \times 0.66322 - e \times 0.79057) \times \frac{c}{V}$$

$$= -4 \times 1.6 \times 10^{-19} \times 0.12735 \times 14.0006 \times 10^{-10}/(2390.9 \times 10^{-30})$$

$$= -4.77\ \mu C/cm^2$$

$$|P_{s1}| = 4.77\ \mu C/cm^2$$

$$P_{s2} = 4 \times (e \times 0.2556 - e \times 0.4346) \times \frac{c}{V}$$

$$= -4 \times 1.6 \times 10^{-19} \times 0.179 \times 14.954 \times 10^{-10}/(2433.1 \times 10^{-30})$$

$$= -7.04\ \mu C/cm^2$$

$$|P_{s2}| = 7.04\ \mu C/cm^2$$

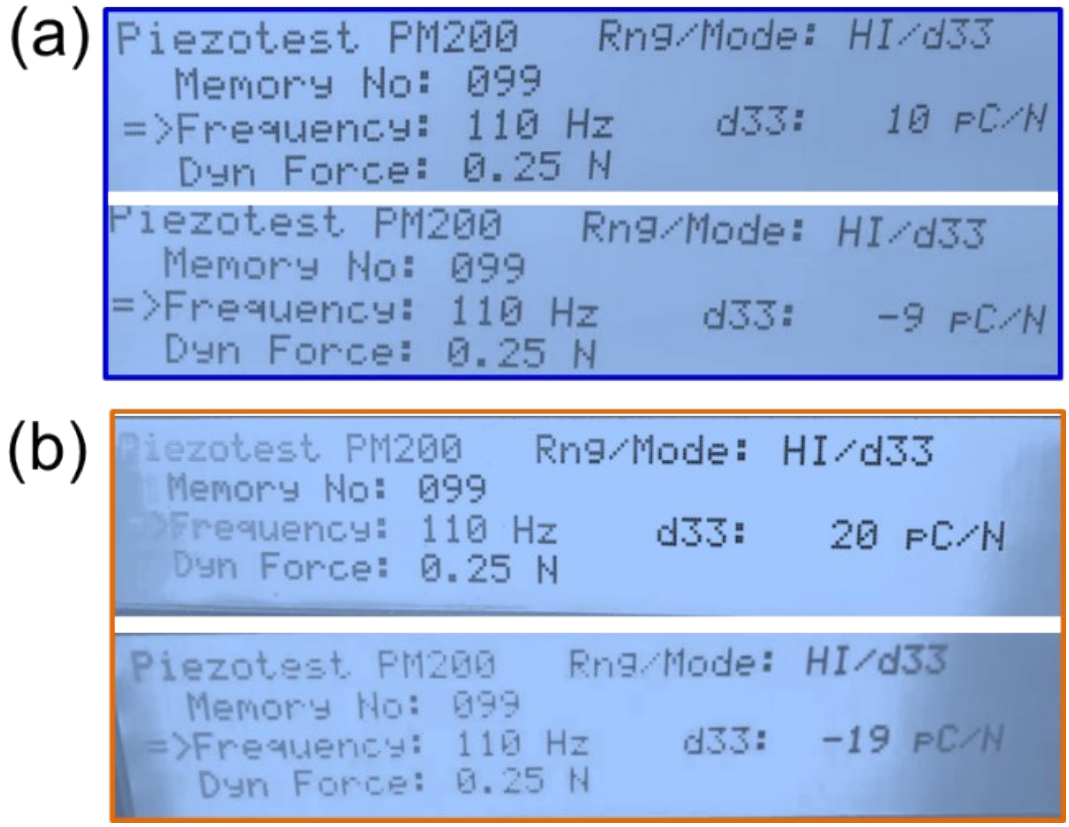

Fig. S9 The photos of piezoelectric measurement for a single crystal of **4** at 293 K (a)

and 370 K (b).

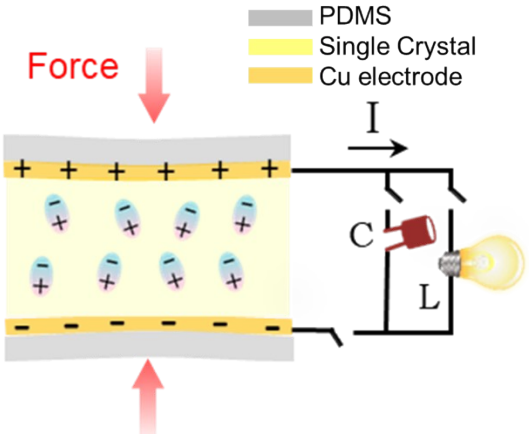

Fig. S10 The schematic diagram of mechano-electronic conversion circuit.

Table S1. The reported crown ether supramolecules showing the polar-to-polar type phase transition

Structure	Chemical name	Low temperature phase	High temperature phase	Phase transition temperature	Piezoelectric coefficient (pC/N) at RT	References
	$[(Me_2N(CH_2)_2NH_3)(18\text{-crown-}6)]ClO_4$	*Pca*2$_1$	*Cmc*2$_1$	364.5	9-20	**This work**
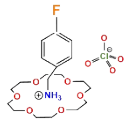	[(4-fluorobenzylammonium)(18-crown-6)]ClO_4	*P*2$_1$	*Cmc*2$_1$	208	—	5
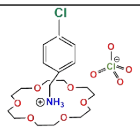	[(4-chlorobenzylammonium)(18-crown-6)]ClO_4	*Pca*2$_1$	*Cmc*2$_1$	172	—	5
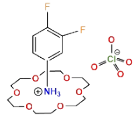	[(3,4-difluoroanilinium)(18-crown-6)] ClO_4	*Pca*2$_1$	*P*2$_1$ or *Pc*	347	—	6
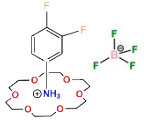	[(3,4-difluoroanilinium)(18-crown-6)] BF_4	*Pca*2$_1$	*P*2$_1$ or *Pc*	361	—	7
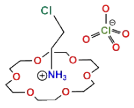	$[(ClCH_2CH_2NH_3)(18\text{-crown-}6)]ClO_4$	*P*2$_1$2$_1$2$_1$	*Pca*2$_1$	363	—	8
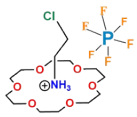	$[(ClCH_2CH_2NH_3)(18\text{-crown-}6)]BF_4$	*P*2$_1$2$_1$2$_1$	*Pca*2$_1$	343	—	8
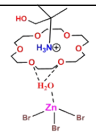	[(2-NH_3-iBuOH)(18-crown-6)][$ZnBr_3(H_2O)$]	*Cc*	*R*3*m*	281	—	9

Table S2. Crystal data and structure refinement for these four supramolecules

Compound	**1**	**2**	**3**	**4**	
Empirical formula	$C_{16}H_{38}Cl_2N_2O_{14}$	$C_{14}Cl_2N_2O_{13}$	$C_{14}H_{33}ClN_2O_9$	$C_{16}H_{37}ClN_2O_{10}$	
Formula weight	553.38	475.06	408.87	452.92	
Crystal system	Monoclinic	Orthorhombic	Orthorhombic	Orthorhombic	Orthorhombic
Space group	$P2_1/c$ (No. 14)	*Pnma* (No. 62)	$P2_12_12_1$ (No. 19)	$Pca2_1$ (No. 29)	$Cmc2_1$ (No. 36)
Temperature (K)	291	293	293	293	368
a (Å)	11.7728(5)	11.547(2)	10.0923(12)	12.8215(7)	12.29(3)
b (Å)	27.5589(9)	10.6358(17)	13.1793(16)	13.3193(10)	13.24(3)
c (Å)	16.5361(8)	20.726(3)	16.253(2)	14.0006(10)	14.95(4)
α (°)	90	90	90	90	90
β (°)	95.487	90	90	90	90
γ (°)	90	90	90	90	90
V (Å^3)	5340.5(4)	2545.4(7)	2161.8(5)	2390.9(3)	2433(10)
Z	8	4	4	4	4
Radiation	Mo-K_α	Mo-K_α	Mo-K_α	Mo-K_α	Mo-K_α
CCDC number	2212389	2212390	2212391	2212392	2212393
Calculated density (g/cm^3)	1.377	1.240	1.256	1.258	1.134
Melting point (K)	418	378	368	421	421
Absorption coefficient (mm^{-1})	0.308	0.311	0.22	0.209	0.213
F (000)	2352	944	880	976	828
Data collection range (°)	3.776-62.224	3.93-50	3.978-49.99	4.41-60.592	4.522-48.992
R (int)	0.0392	0.0686	0.057	0.0179	0.1619
Completeness to θ	0.841	1.0	1.69/0.96	1.07/0.56	1.79/0.94
Data, restraints, parameters	14448, 396, 628	2369, 79, 190	3670, 146, 239	3987, 1, 266	2012, 174, 167
Goodness-of-fit on F^2	1.071	1.049	0.89	1.069	1.014
R_1, $wR_2[I > 2\sigma(I)]$	0.1485, 0.2258	0.1598, 0.2942	0.0983, 0.2986	0.0414, 0.1231	0.1932, 0.4123
$\Delta\rho_{max}$, $\Delta\rho_{min}$ (e Å^{-3})	0.64, -0.42	0.44, -0.41	0.35, -0.25	0.34, -0.23	0.35, -0.38

References

1. J. P. Perdew, M. Ernzerhof and K. Burke, Rationale for mixing exact exchange with density functional approximations, *J. Chem. Phys.*, 1996, **105**, 9982-9985.
2. Y. Q. Li, J. H. Luo and S. E. Zhao, Local polarity-induced assembly of second-order nonlinear optical materials, *Acc. Chem. Res.*, 2022, **55**, 3460-3469.

3. L. Kang, F. Liang, X. Jiang, Z. Lin and C. Chen, First-principles design and simulations promote the development of nonlinear optical crystals, *Acc. Chem. Res.*, 2020, **53**, 209-217.
4. X. Jiang, S. Luo, L. Kang, P. Gong, H. Huang, S. Wang, Z. Lin and C. Chen, First-principles evaluation of the alkali and/or alkaline earth beryllium borates in deep ultraviolet nonlinear optical applications, *ACS Photonics*, 2015, **2**, 1183-1191.
5. F. Jiang, C. F. Wang, Y. X. Wu, H. H. Li, C. Shi, H. Y. Ye and Y. Zhang, Nonlinear optical and photoluminescence bistable responses accompanied by tunable dielectric behaviors in crown inclusions, *J. Phys. Chem. C*, 2020, **124**, 5796-5801.
6. Y. L. Wei, J. Jing, C. Shi, H. Y. Ye, Z. X. Wang and Y. Zhang, Unusual high-temperature reversible phase transition containing dielectric and nonlinear optical switches in host-guest supramolecular crown ether clathrates, *Chem. Commun.*, 2018, **54**, 8076-8079.
7. J. Jing, C. Shi, H.-Y. Ye and Y. Zhang, Tunable relaxation type and switch type response triggered by phase transition in 3,4-difluoroanilinium 18-crown-6 tetrafluoroborate, *Inorg. Chem. Commun.*, 2019, **103**, 67-71.
8. Y.-F. Gao, Z.-X. Zhang, T. Zhang, C.-Y. Su, W.-Y. Zhang and D.-W. Fu, Regulated molecular rotor in phase transition materials with switchable dielectric and SHG effect, *Mater. Chem. Front.*, 2020, **4**, 3003-3012.
9. W. Li, D. X. Liu, W. Y. Hu, Q. Y. Liu, Z. Y. Du, C. T. He, W. X. Zhang and X. M. Chen, A crystalline supramolecular rotor functioned by dual ultrasmall polar rotators, *Chinese J. Chem.*, 2022, **40**, 1917-1923.